J Adv Ceram

Research Article

Enhanced tribocatalysis through combining charge transfer with electron jumping in co-doped NiO magnetic nanocatalyst for water purification

Ruihua Mu[1], Xiaoqian Shi[1], Zheng Wu[1,✉], Siqi Hong[1], Huijuan Li[1], Wenbao Yang[1], Yunhong Li[1,✉], Wenwen Liu[3], Najun Li[4], Changchun Hao[2], Gangqiang Zhu[2], Wanping Chen[5], Yanmin Jia[2,✉]

Cite this article: Mu R, Shi X, Wu Z, et al. *J Adv Ceram* 2026, **15**(5): 9221279. https://doi.org/10.26599/JAC.2026.9221279

ABSTRACT: Mechanical friction energy is a ubiquitous green energy that can be collected and transformed into electrical energy for water treatment, a concept theoretically referred to as tribocatalysis. The efficient removal of organic pollutants from wastewater by tribocatalysis still faces challenges. Employing doping technology to introduce metallic elements into materials is anticipated to enhance tribocatalytic performance by improving material properties. In this work, NiO and *x* wt% Co-doped NiO (*x* = 3, 5, 7, and 9) nanocatalysts are prepared using a coprecipitation method. The incorporation of Co effectively reduces the bandgap of NiO, enhancing tribocatalytic decomposition performance through the synergistic effects of charge transfer and electron transition. Notably, the optimized 7 wt% Co–NiO nanoparticles demonstrate the leading performance in the decomposition of rhodamine B (RhB), with a decomposition ratio of 96.7% after 120 min, representing a 23.1% increase over pure NiO. Electrochemical impedance spectroscopy (EIS) demonstrates that Co doping reduces the charge transfer resistance of NiO, resulting in the production of more reactive species. Radical trapping experiments and electron paramagnetic resonance spectroscopy (ESR) reveal that both superoxide radicals ($\cdot O_2^-$) and holes (h^+) are key active radicals in dye decomposition. Furthermore, the 7 wt% Co–NiO nanocatalyst exhibits excellent stability and magnetic recyclability, retaining an 87.1% decomposition ratio after five cycles. The Co–NiO nanocatalyst, with these advantages of excellent tribocatalysis performance, low cost, and magnetic recyclability, has potential for application in wastewater treatment through harvesting and utilizing environmental mechanical friction energy in the future.

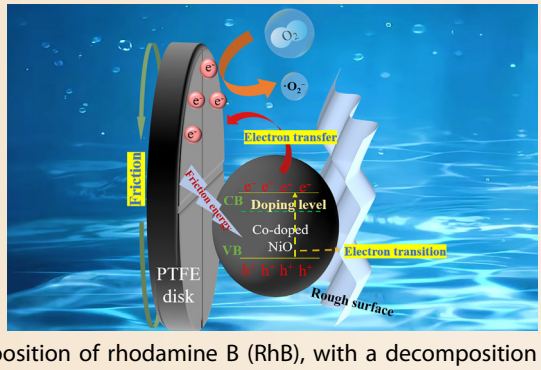

KEYWORDS: tribocatalysis; Co–NiO; harvesting friction energy; water purification

1 Introduction

Environmental pollution and energy shortages are becoming increasingly serious, not only threatening human health but also potentially hindering long-term stable economic development [1]. Therefore, there is a strong push for green catalytic technology to tackle this dual challenge. Recently, cutting-edge catalytic methods, including photocatalysis, piezocatalysis, and pyrocatalysis, have gained attention for their extraordinary ability to tap solar, mechanical, or thermal energy and convert it into chemical energy, paving the way for innovative environmental cleanup solutions [2–4]. Among these, photocatalytic technology uses semiconductors that, in the presence of light, generate electron–hole pairs that are then used to catalyze reactions [5]. However, photocatalytic efficiency is typically low due to poor light utilization efficiency and severe electron–hole recombination [6]. Pyrocatalysis requires precise control of temperature changes to trigger reactions [7]. However, this inherent difficulty poses significant challenges for its practical application. Mechanical energy is ubiquitous in nature. Piezocatalysis is a process in which mechanical vibration is applied to a piezoelectric material, generating polarized charges and an internal electric field that drives catalytic reactions to decompose organic pollutants [8]. However, the high-frequency ultrasonic vibrations essential for piezocatalytic reactions are rare in natural environments [9,10].

Tribocatalysis has recently been developed as a cutting-edge

[1] School of Environmental and Chemical Engineering, Key Laboratory of Functional Textile Material and Product, Ministry of Education, Xi'an Polytechnic University, Xi'an 710048, China. [2] Quantum Materials and Devices Key Laboratory of Shaanxi Province's High Education Institution, School of Physics and Information Technology, Shaanxi Normal University, Xi'an 710119, China. [3] College of Intelligent Manufacturing and Materials & Chemical Engineering, Yichun University, Yichun 336000, China. [4] College of Chemistry, Chemical Engineering and Materials Science, Collaborative Innovation Center of Suzhou Nano Science and Technology, Soochow University, Suzhou 215123, China. [5] School of Physics and Technology, Wuhan University, Wuhan 430072, China.

✉ Corresponding authors. E-mail: Z. Wu, wuzheng@xpu.edu.cn; Y. Li, liyunhong@xpu.edu.cn; Y. Jia, ymjia@snnu.edu.cn

Received: January 6, 2026; Revised: February 15, 2026; Accepted: March 8, 2026

catalytic technique. Tribocatalysis is a process that utilizes the positive and negative charges generated via the triboelectric effect when materials with significantly different triboelectric polarities undergo sliding contact, thereby driving catalytic reactions for the decomposition of organic pollutants [11]. Considering that any two different materials rubbing against each other are electrically charged, there is a wide range of tribocatalysts to choose from. In 2019, Li *et al.* [12] initially reported that $Ba_{0.75}Sr_{0.25}TiO_3$ nanoparticles can be used for dye decomposition through tribocatalysis. Subsequently, a variety of catalysts, including ZnO [13], $BaTiO_3$ [14], TiO_2 [15], $BiVO_4$ [16], $CaCu_3Ti_4O_{12}$ [17], and $NiCo_2O_4$ [18], have been developed for tribocatalysis. Despite the increasing research on tribocatalysis, its performance improvement still faces great challenges.

A crucial factor in enhancing tribocatalytic performance is accelerating the charge transfer rate [19]. Doping other substances in materials is considered an effective method for enhancing charge transfer [20]. For example, Liu *et al.* [21] doped Sr into $BaTiO_3$ and demonstrated that Sr doping enhanced the charge separation capability, thereby promoting its tribocatalytic performance. Hu *et al.* [22] also prepared Fe-doped ZnO for the tribocatalytic decomposition of rhodamine B (RhB) and indicated that the decomposition ratio of RhB increased from 53.4% to 91.6% with Fe modification. Fe doping introduced both impurity energy levels and extra electrons into ZnO, lowering its work function. The reduction in work function promotes charge separation, enabling easier electron movement under tribocatalysis and thereby boosting catalytic performance.

NiO, an abundant and environmentally benign transition metal oxide, is widely employed in diverse areas, such as catalysis, sensing, and optoelectronics, owing to its excellent electrical conductivity, thermal stability, and photoresponsiveness [23]. Its combination of practicality and sustainable supply makes NiO particularly valuable in modern materials science [24]. In addition, NiO is magnetic and easy to recycle after reaction [25]. However, the band potential of the NiO semiconductor catalyst is wide, measuring between 3.6 and 4.0 eV [26]. It takes more energy to complete carrier separation [27]. Theoretically, doping metal elements into NiO introduces impurity energy levels and optimizes its electron distribution, which enhances the electron transfer capacity and consequently enhances tribocatalytic performance [28].

In this work, Co–NiO nanoparticles with different Co contents were synthesized by a coprecipitation method. The tribocatalytic decomposition of RhB by x wt% Co–NiO under mechanical stirring was studied, with an efficiency of 7 wt% Co–NiO reaching 96.7% within 120 min. The relevant decomposition rate constant (k = 0.02613 min^{-1}) is approximately 2.4 times that of pure NiO (k = 0.01084 min^{-1}). The recycling experiment verifies the universality and durability of the Co–NiO tribocatalyst. The effect of Co doping on the energy band structure of NiO was systematically analyzed, based on which a mechanism for tribocatalytic dye decomposition was proposed. This progression enables the utilization of widespread environmental friction energy for wastewater treatment.

2 Experimental

2.1 Materials

Nickel(II) chloride hexahydrate ($NiCl_2{\cdot}6H_2O$), cobalt(II) chloride hexahydrate ($CoCl_2{\cdot}6H_2O$), sodium hydroxide (NaOH), rhodamine B (RhB), methyl orange (MO), methylene blue (MB), poly(vinylidene fluoride) (PVDF), *N*-methyl-2-pyrrolidone (NMP), tert-butyl alcohol (TBA), benzoquinone (BQ), ethylene diamine tetraacetic acid (EDTA), 5,5-dimethyl-1-pyrroline N-oxide (DMPO), methanol (CH_3OH), and 2,2,6,6-tetramethylpiperidinamine (TEMPO) were purchased from Anhui Senrise Technologies Co., Ltd. All reagents were of analytical grade quality.

2.2 Synthesis of NiO and Co–NiO nanoparticles

NiO and Co–NiO nanoparticles were synthesized via the coprecipitation method. $NiCl_2{\cdot}6H_2O$ (1.54 g) was mixed with 40 mL of deionized water, followed by stirring until a consistent mixture was achieved. $CoCl_2{\cdot}6H_2O$ with different amounts was introduced into the solution. After 30 min, 1 M NaOH was added to the mixed solution until precipitation was complete. Subsequently, stirring continued for 2 h at 60 °C to produce a mixed slurry. The filtered slurry precipitate was oven-dried for 12 h after washing, followed by calcination at 550 °C for 3 h. NiO and x wt% (x = 3, 5, 7, and 9) Co–NiO nanoparticles were harvested.

2.3 Material characterization

An X-ray diffractometer (XRD; D8 Advance, Germany) technique verified the phase structure. Surface morphology was analyzed by a scanning electron microscope (SEM; Hitachi SU8010, Japan). The specific surface area (S_{BET}) and pore structure of the samples were measured by the Brunauer–Emmett–Teller (BET) method on an Autosorb iQ analyzer (USA). The RhB dye absorbance was measured with an ultraviolet–visible (UV–Vis) spectrophotometer (Techcomp, UV2300II, China). The elemental composition of the sample was analyzed using an X-ray photoelectron spectrometer (XPS; Kratos AXIS SUPRA+, Japan). An electron spin resonance spectrometer (ESR; Bruker EMXnano, Germany) was utilized to probe the active species. EIS measurements were conducted using an electrochemical workstation (CHI650E, Shanghai CH Instruments Co., Ltd., China).

2.4 Tribocatalysis experiment

Co–NiO nanoparticles (200 mg) were added to 30 mL of RhB and stirred with a polytetrafluoroethylene (PTFE) disk at room temperature under dark conditions. The supernatant was taken to measure the absorbance at regular intervals, and the decomposition ratio of the dye was calculated by Eq. (1) [29]:

$$D = (1 - A/A_0) \times 100\% \quad (1)$$

where A is the absorbance of the dye in the decomposition process; A_0 is the absorbance of the undecomposed dye; D is the decomposition ratio of the dye.

2.5 Active species experiment

Active species inhibition assays are widely used to reveal the regime of dye decomposition. TBA, EDTA-2Na, and BQ were used as suppressants of hydroxyl radicals (·OH), holes (h^+), and superoxide radicals ($\cdot O_2^-$). The effect of suppressant addition on the decomposition performance of dyes was investigated by adding 2 mM scavenger to RhB solution containing Co–NiO nanoparticles, and the active species produced was further investigated by employing ESR.

2.6 ESR assay for active species experiment

5 mL of deionized water and 5 mL of CH_3OH were poured into two beakers containing 200 mg of Co–NiO and 0.05 mL of DMPO, respectively. The mixture was mechanically stirred at

600 r·min^{-1} using a PTFE disk. The suspension was analyzed by ESR to identify ·OH and ·O_2^- after a certain stirring time. 5 mL of deionized water was added to a glass beaker containing Co–NiO nanoparticles and 0.05 mL of TEMPO, and h^+ formation was examined by the same method.

2.7 EIS testing

First, Co–NiO nanoparticles (50 mg) were mixed with PVDF (40 mg). The mixture was thoroughly ground. Subsequently, NMP (400 μL) was added, after which the blend was stirred for 30 min. Finally, the mixed solution was applied to the surface of FTO glass (10 mm × 20 mm) and desiccated at 60 °C. The resulting samples were used for the EIS test using a standard three-electrode system (Pt counter electrode, sample-coated FTO working electrode, and saturated calomel reference electrode) of an electrochemical workstation.

3 Results and discussion

3.1 Characterization of NiO and Co–NiO nanoparticles

The XRD patterns of the as-synthesized NiO and *x* wt% (*x* = 3, 5, 7, and 9) Co–NiO are shown in Fig. 1(a). All samples exhibit a hexagonal phase with an $Fm\bar{3}m$ space group (JCPDS Card No. 44-1159) [30], indicating the absence of structural changes after Co doping. The progressive shift of the enlarged (111) peak at 2θ = 36°–38° toward lower angles with increasing Co content, as shown in Fig. 1(b), is ascribed to the replacement of the smaller Ni^{2+} (0.605 Å) by the larger Co^{2+} (0.621 Å), resulting in an increased lattice constant [31]. The above results suggest that Co ions can partially displace Ni ions with similar ionic radii and are well incorporated into the NiO lattice.

The morphological characteristics of NiO and 7 wt% Co–NiO nanoparticles were investigated using SEM. As shown in Fig. 2(a), the NiO nanoparticles are spherical with some agglomeration. The particle size dispersion of NiO nanoparticles is statistically analyzed, as shown in Fig. 2(b). The particle size of the NiO nanoparticles is mainly concentrated in the 40–120 nm range, with an average particle size of ~75 nm. Figure 2(c) shows the uniformly dispersed grain structure in 7 wt% Co–NiO nanoparticles. There is no change in the morphology of 7 wt% Co–NiO compared with that of the undoped NiO. Dopants enable significant modulation of NiO crystal growth, thereby controlling the final sample size. Through statistical analysis of the particle size dispersion of the Co–NiO nanoparticles, as shown in Fig. 2(d), the particle size of the Co–NiO nanoparticles is mainly concentrated in the 30–80 nm range, and the average size of the particles is ~48 nm. Co doping in NiO nanoparticles introduces lattice strain, which inhibits crystal growth, thereby reducing particle size and improving size uniformity [32].

XPS characterized the elemental components of the prepared NiO and 7 wt% Co–NiO. The survey spectra are shown in Fig. 3(a). Elemental analysis of 7 wt% Co–NiO via survey scans confirms the existence of Ni, O, and Co. The Co 2p high-resolution spectrum is shown in Fig. 3(b). The deconvoluted peaks at 780.44 eV (Co $2p_{3/2}$) and 795.57 eV (satellite) confirm the Co^{2+} oxidation state. The high-resolution O 1s spectrum is shown in Fig. 3(c). Three peaks located at 528.77, 530.50, and 532.43 eV are assigned to lattice oxygen (Ni–O), oxygen vacancies or metal deficiencies, and adsorbed oxygen species (O–H) bonds, respectively [33]. The high-resolution Ni 2p spectrum is shown in Fig. 3(d). The Ni $2p_{3/2}$ peaks occur at 854.01, 856.09, and 861.10 eV, corresponding to $Ni^{\delta+}$ ($0 > \delta > 2$), Ni^{2+}, and its satellite. Ni $2p_{1/2}$ peaks at 872.21 and 879.22 eV indicate Ni^{2+} and its satellite [34].

The specific surface area of the catalyst generally influences its catalytic performance. As shown in Fig. 4, the N_2 adsorption–desorption isotherms for NiO and 7 wt% Co–NiO show a characteristic type *IV* pattern. The hysteresis between adsorption and desorption branches at $0.8 \le P/P_0 \le 1.0$—where *P* denotes the equilibrium adsorption pressure and P_0 the saturated vapor pressure at the experimental temperature—demonstrates that the catalyst possesses a mesoporous structure [35]. This is additionally substantiated by the pore size distribution curves, in which d*V*/d*D* represents the rate of change of pore volume with pore diameter. The specific surface area and pore volume of 7 wt% Co–NiO are 27.0410 $m^2 \cdot g^{-1}$ and 19.98 $mm^3 \cdot g^{-1}$, respectively, which are higher than those of NiO (22.6084 $m^2 \cdot g^{-1}$ and 16.67 $mm^3 \cdot g^{-1}$, respectively). The catalytic reactions are significantly enhanced owing to the abundant active sites provided by large specific surface area of the catalyst. The presence of mesopores contributed to reduced diffusion resistance and enhanced the availability of active sites.

3.2 Tribocatalytic performance of NiO and *x* wt% Co–NiO nanoparticles

The tribocatalytic performance of NiO and *x* wt% Co–NiO nanoparticles was evaluated by measuring the decomposition ratio

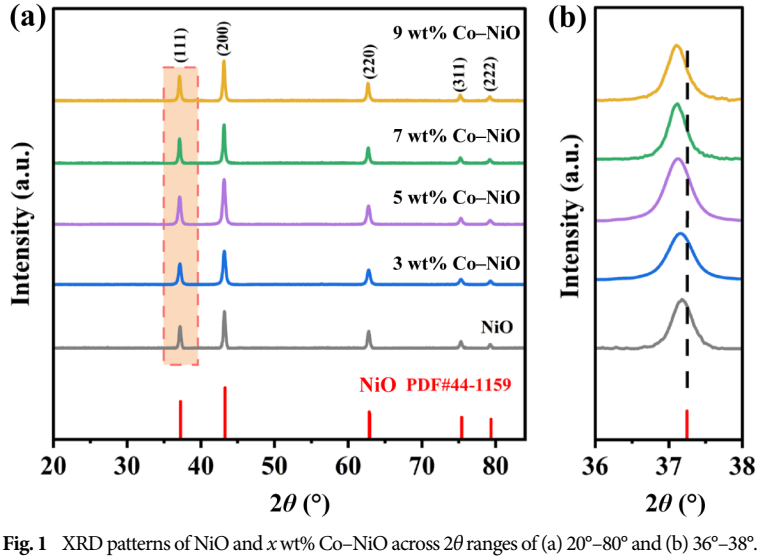

Fig. 1 XRD patterns of NiO and *x* wt% Co–NiO across 2θ ranges of (a) 20°–80° and (b) 36°–38°.

清華大学出版社 Tsinghua University Press | SciOpen

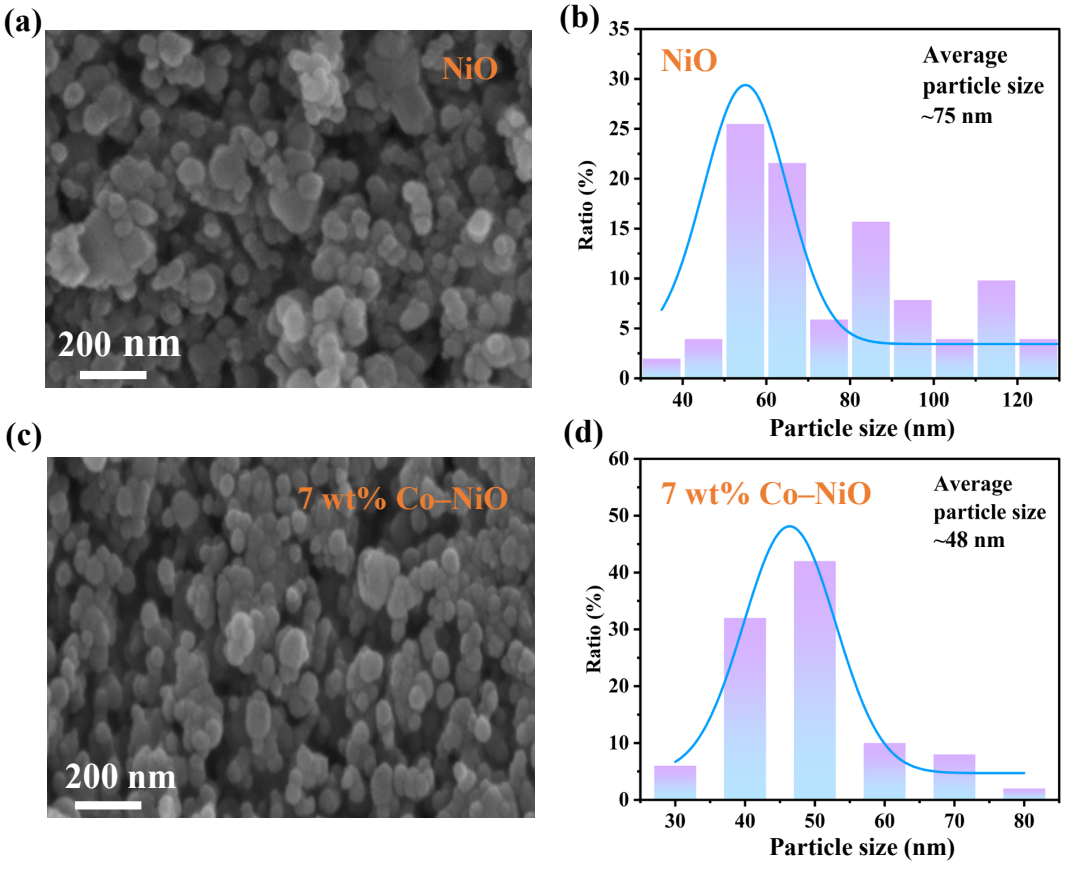

Fig. 2 (a) SEM images and (b) size distribution of NiO nanoparticles. (c) SEM images and (d) size distribution of 7 wt% Co–NiO nanoparticles.

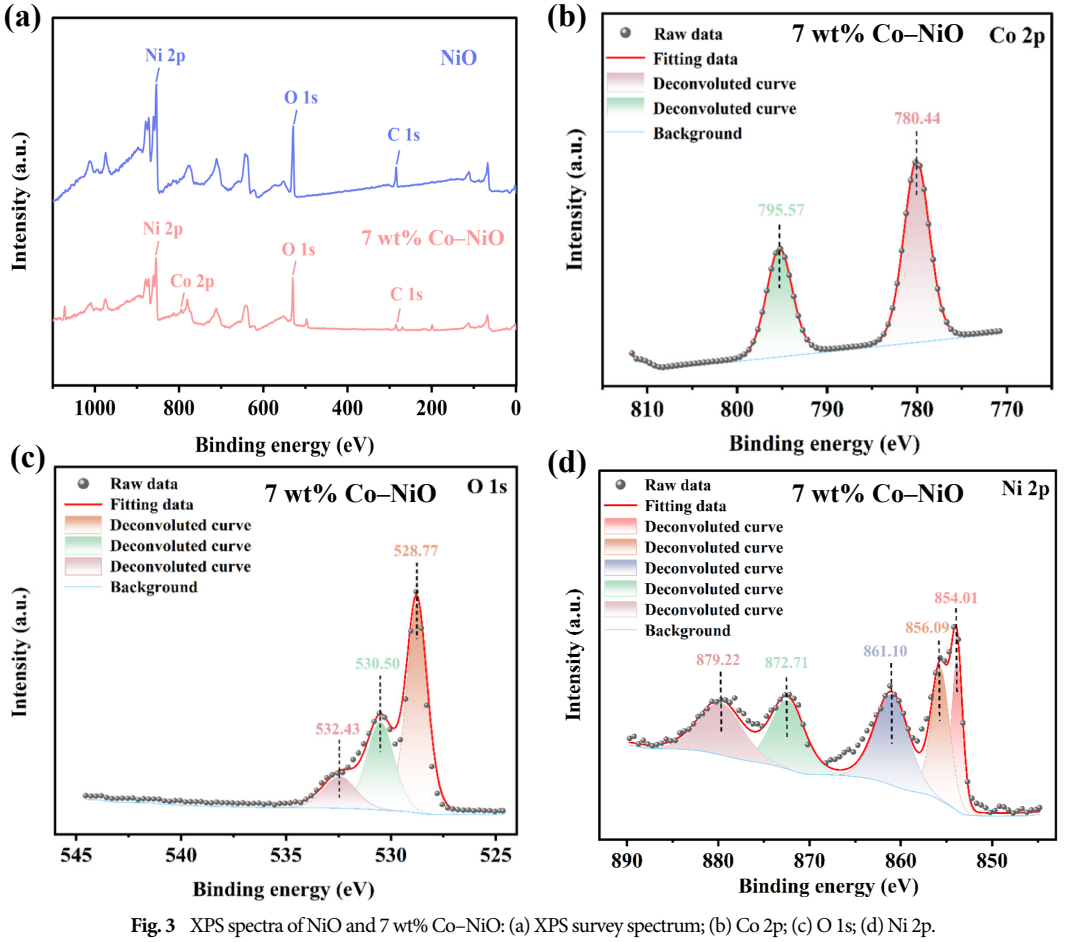

Fig. 3 XPS spectra of NiO and 7 wt% Co–NiO: (a) XPS survey spectrum; (b) Co 2p; (c) O 1s; (d) Ni 2p.

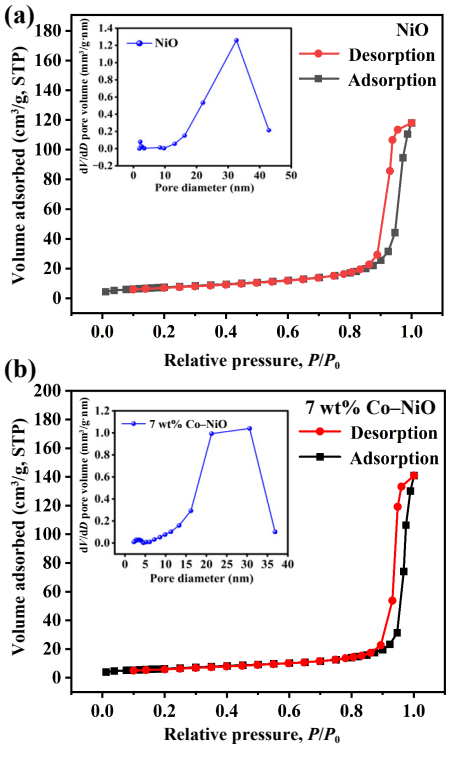

Fig. 4 N_2 adsorption–desorption isotherms and pore-size distributions (inset) for (a) NiO and (b) 7 wt% Co–NiO.

of RhB under dark conditions using a mechanically stirred PTFE disk at 600 r·min^{-1}. As clearly shown in Fig. 5(a), the dye decomposition ratios for NiO, 3 wt% Co–NiO, 5 wt% Co–NiO, 7 wt% Co–NiO, and 9 wt% Co–NiO are 73.6%, 87.4%, 89.5%, 96.7%, and 85.3% (reaction for 120 min), respectively. Subsequently, the reaction rate is evaluated through fitting data using the pseudo-first-order kinetics mode as expressed in Eq. (2) [36]:

$$\ln(A_0/A) = kt \tag{2}$$

where k represents the rate constant and t is the reaction time. The k values for NiO, 3 wt% Co–NiO, 5 wt% Co–NiO, 7 wt% Co–NiO, and 9 wt% Co–NiO in Fig. 5(b) are 0.01084, 0.01659, 0.01806, 0.02613, and 0.01552 min^{-1}, respectively. With the growth of the Co doping amount, the decomposition ratio of RhB increases, followed by a decrease. When the Co content is 7 wt%, the decomposition ratio of RhB reaches the maximum. The 7 wt% Co–NiO nanoparticles exhibit a decomposition ratio of RhB approximately 2.4 times higher than that of pure NiO. This enhancement stems from Co doping promoting carrier separation and charge transfer efficiency in NiO. However, excessive Co doping can lead to severe recombination of hole–electron pairs, thereby reducing tribocatalytic performance [37].

The effect of stirrer speed on dye decomposition efficiency is systematically evaluated. The RhB decomposition ratios of 7 wt% Co–NiO with stirring speeds of 200, 400, 600, and 800 r·min^{-1} are 49.8%, 79.8%, 96.7%, and 92.1%, respectively (Fig. 6(a)). The decomposition rate constant of RhB increased with increasing

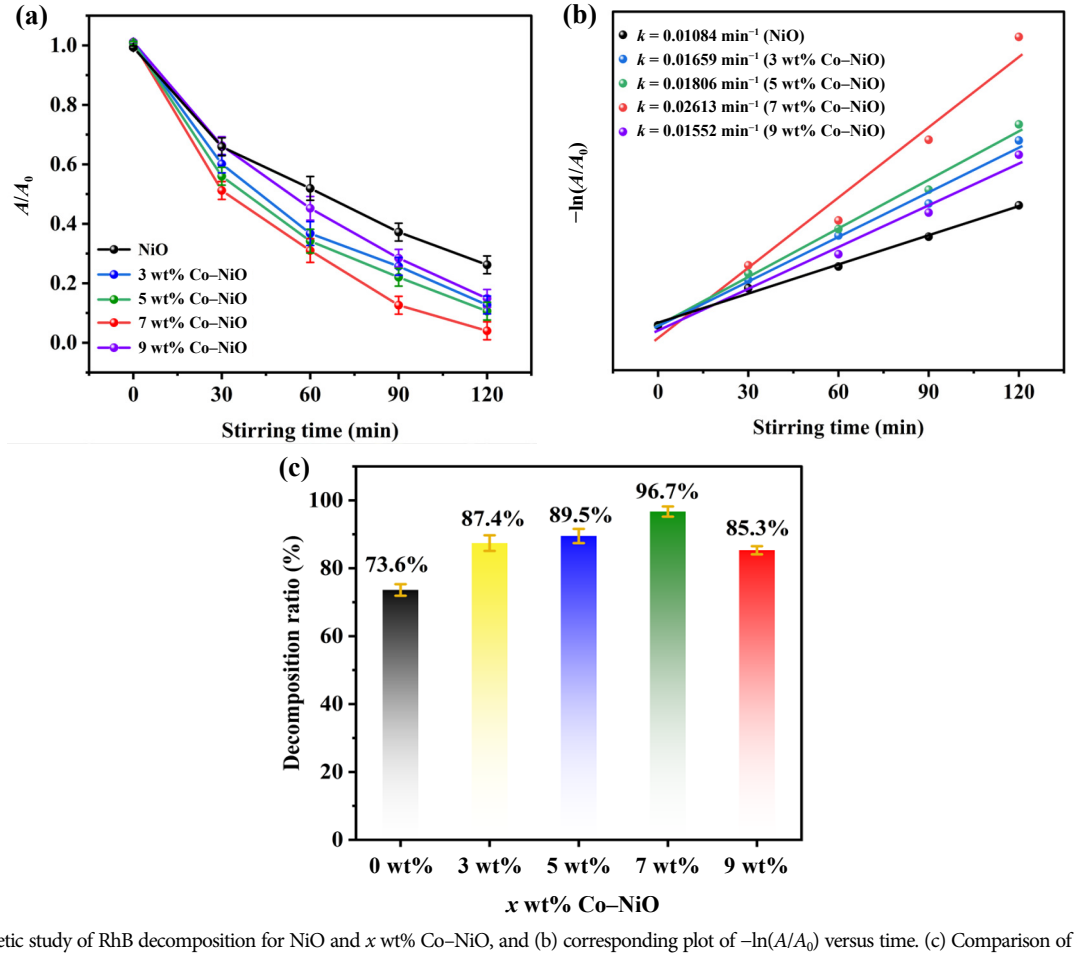

Fig. 5 (a) Kinetic study of RhB decomposition for NiO and x wt% Co–NiO, and (b) corresponding plot of $-\ln(A/A_0)$ versus time. (c) Comparison of decomposition ratios of NiO and x wt% Co–NiO on RhB after 120 min.

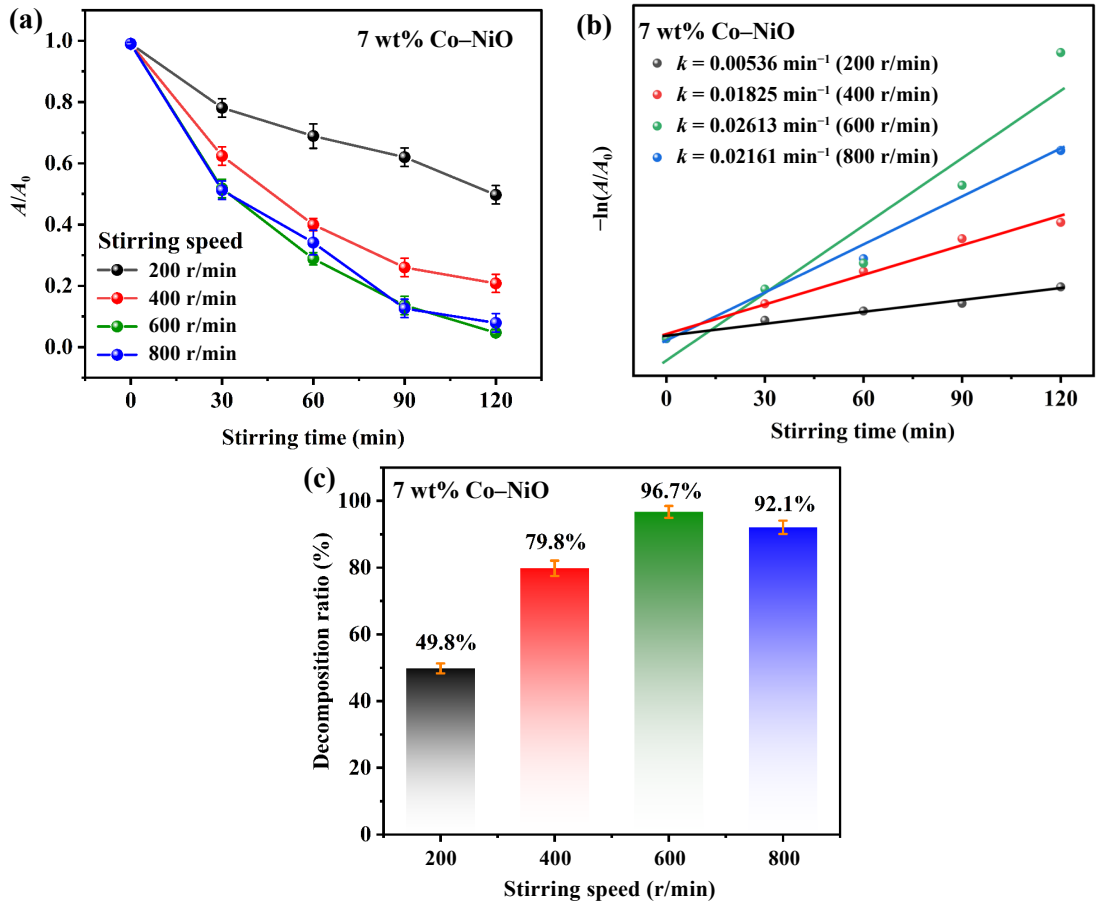

Fig. 6 (a) Impact of stirring speed on RhB decomposition ratio via 7 wt% Co–NiO nanoparticles and (b) corresponding plot of $-\ln(A/A_0)$ versus time. (c) Comparison of decomposition ratios of NiO and 7 wt% Co–NiO on RhB at different stirring speeds.

PTFE disk stirring speed from 200 to 600 r·min^{-1}, reaching a maximum value of 1.3×10^{-1} min^{-1} at 600 r·min^{-1} (Fig. 6(b)). The observed enhancement is attributed to the elevated stirring speed, which promotes dye molecule migration to the catalyst surface and thereby increases the interaction frequency with active sites, enhancing the overall catalytic efficiency [38]. The decline in RhB decomposition ratios at excessive stirring speeds should probably be attributed to catalyst loss caused by the compromised rotational stability of the PTFE disk [39]. Therefore, the decomposition ratio at 800 r·min^{-1} is lower than that at 600 r·min^{-1}.

The interfacial contact area between PTFE and the bottom of the beaker is a significant factor during RhB decomposition under mechanical stirring. The contact area is varied by altering the shape of PTFE, as shown in Fig. 7. The contact areas of the PTFE disk, cylinder, and shuttle with the bottom of the beaker are 240, 60, and 4 mm^2, respectively. The decomposition ratios of RhB with the three shapes of PTFE are 96.7%, 48.8%, and 45.6% within 2 h, respectively. By increasing the PTFE-beaker contact area, more catalysts are concentrated at the interface. This promotes a higher frequency of effective friction, driving the enhancement in tribocatalytic performance.

The decomposition ratios of different organic contaminants as evaluation indicators are determined to test the environmental universality of the 7 wt% Co–NiO nanoparticles, as shown in Fig. 8. The decomposition ratios of MB (75.3%) and MO (16.2%) are less than that of RhB (96.7%). The breakdown of the distinct chemical bonds in different dye molecules usually requires a specific amount of energy. In the RhB molecule, the primary

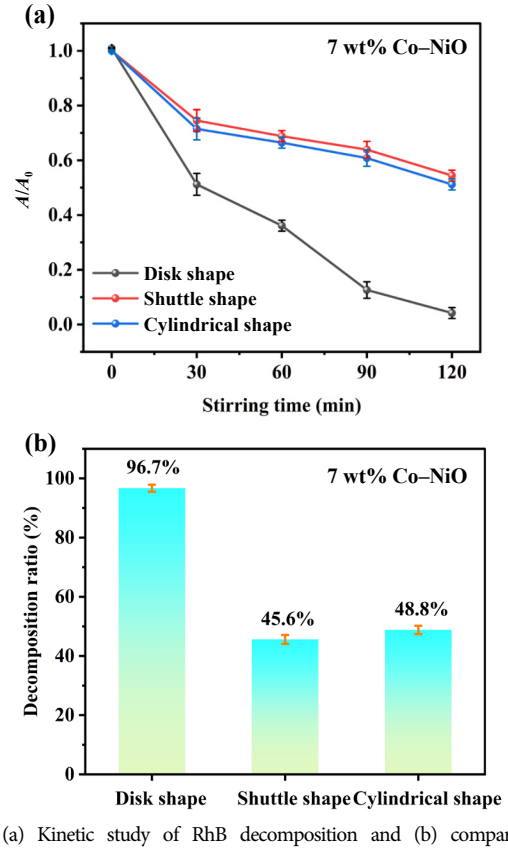

Fig. 7 (a) Kinetic study of RhB decomposition and (b) comparison of decomposition ratios for 7 wt% Co–NiO using different PTFE shapes.

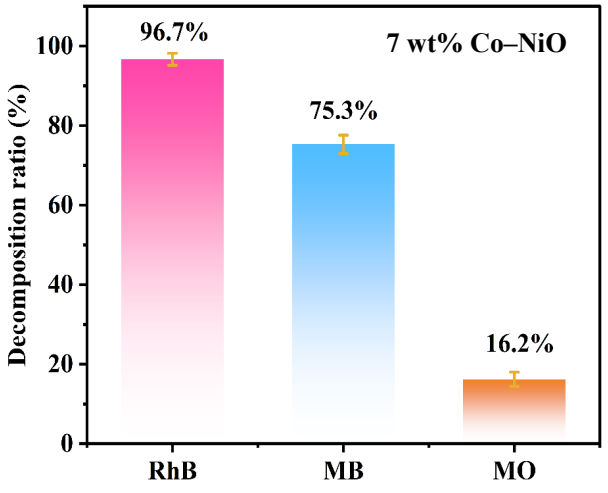

Fig. 8 Tribocatalytic decomposition ratio of MO, MB, and RhB using 7 wt% Co–NiO nanoparticles.

bonds are C–N and C–C, which are prone to breaking. This accounts for the molecule's high decomposition ratio. In contrast, the lower decomposition ratios of MB and MO are due to the existence of C=N and N=N bonds, which require higher energies to break than C–C bonds [40]. These results show that 7 wt% Co–NiO nanoparticles have general applicability against different pollutants.

The recyclability of catalysts is an important indicator to evaluate their stability in water treatment. As depicted in Figs. 9(a) and 9(b), because the Co-doped NiO is magnetic, it allows for easy separation and recycling. Figure 9(c) shows that the 7 wt% Co–NiO nanoparticles maintain stable tribocatalytic performance after five consecutive cycles, with a decomposition ratio of 87.1%. XRD analysis of the 7 wt% Co–NiO nanoparticles (Fig. 9(d)) revealed no change in the characteristic peaks, validating their excellent cyclability and reusability.

4 Role of Co doping in enhancing tribocatalysis

It has been proposed that the tribocatalytic mechanism could proceed via electron transfer or leaps, with both pathways potentially operating concurrently [41]. Since NiO is a semiconductor, its electronic structure can absorb energy effectively to produce electron–hole pairs [42]. The UV–Vis spectra (Fig. 10(a)) reveal that Co doping extends the light-absorption range of NiO and improves its responsiveness to external excitation, thereby contributing to the observed improvement in tribocatalytic performance. The data from the UV–Vis spectra are transformed using Tauc's equation (Eq. (3)) [43]:

$$(\alpha h\nu)^m = A(h\nu - E_g) \tag{3}$$

where α is the absorption coefficient; h is Planck's constant; ν is the frequency of the incident photon; A is a constant; E_g represents the band gap energy. The exponent m is determined by the nature of the optical transitions. For NiO, a direct band gap semiconductor, m is taken as 2 [44]. The Tauc plot derived from Eq. (3) is shown in Fig. 10(b). The band gap widths for the pure NiO and 7 wt% Co–NiO nanoparticles were 3.09 and 2.81 eV, respectively. Co doping effectively reduces the band gap of NiO, which consequently enhances the carrier separation efficiency.

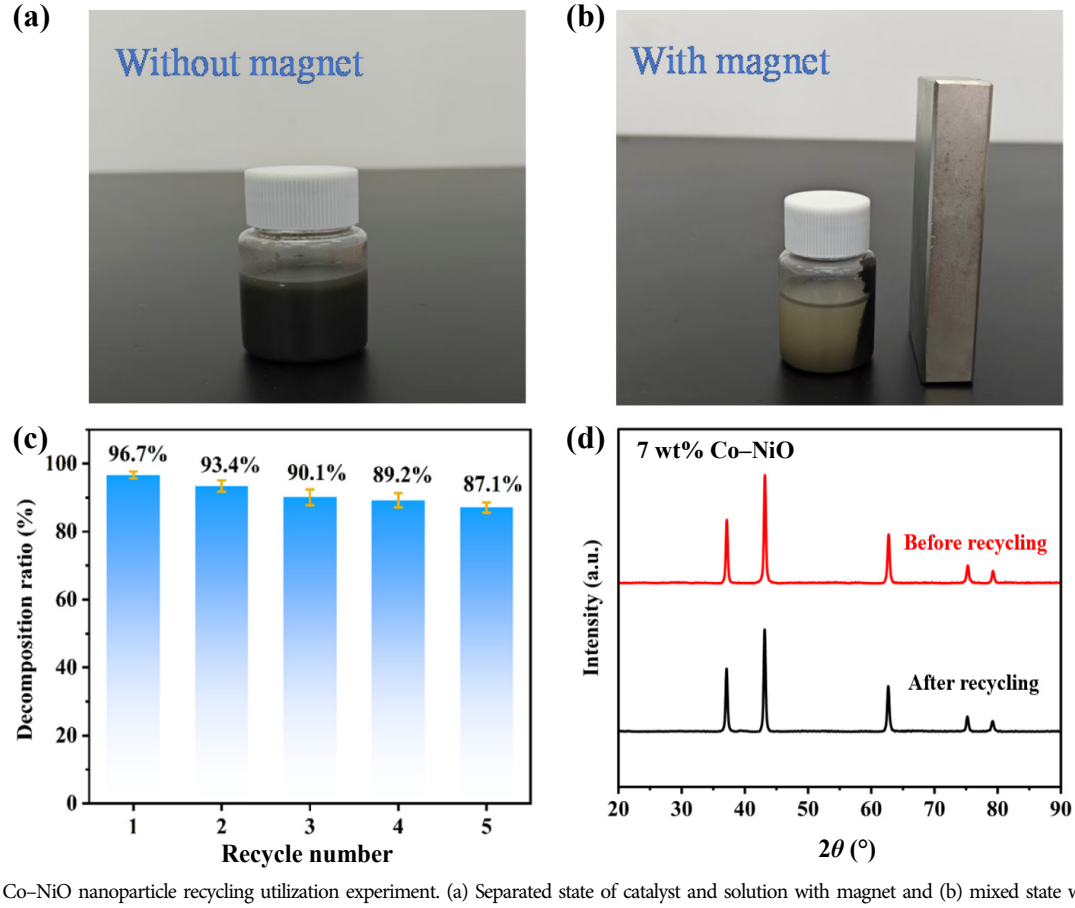

Fig. 9 7 wt% Co–NiO nanoparticle recycling utilization experiment. (a) Separated state of catalyst and solution with magnet and (b) mixed state without magnet. (c) RhB dye decomposition ratio and (d) XRD patterns of 7 wt% Co–NiO nanoparticles after five recycling experiments.

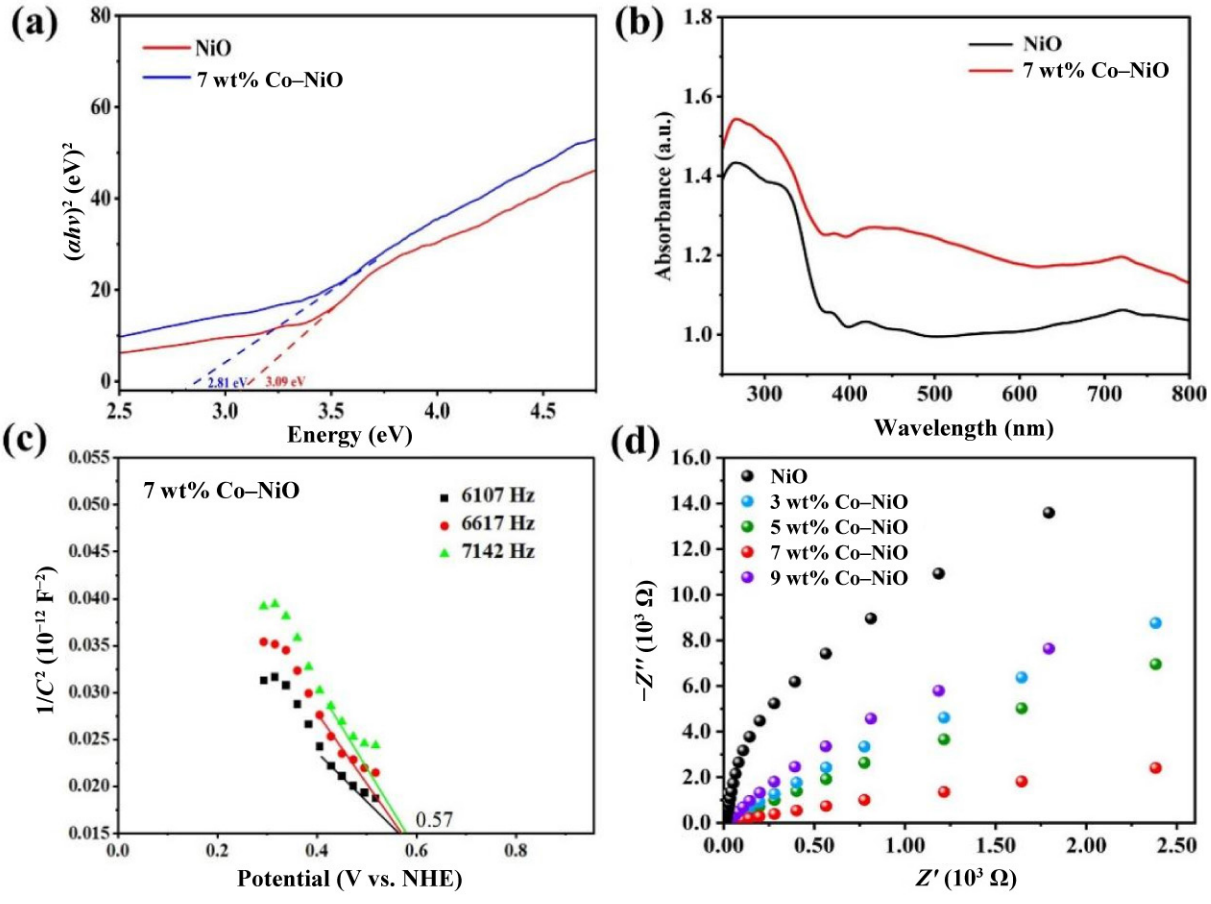

Fig. 10 (a) UV–Vis absorption spectra of NiO and 7 wt% Co–NiO. (b) Band gap and (c) Mott–Schottky curves of 7 wt% Co–NiO. (d) Electrochemical impedance spectroscopy of *x* wt% Co–NiO.

Figure 10(c) shows the Mott–Schottky curves of 7 wt% Co–NiO. The negative slope of the 7 wt% Co–NiO curve indicates that it is a p-type semiconductor, whose valence band energy (E_{VB}) is close to the flat-band potential. The E_{VB} is calculated to be 0.57 eV using the standard hydrogen electrode equation. The E_{CB} was calculated as 2.24 eV using the empirical equation (Eq. (4)) [45]:

$$E_g = E_{VB} - E_{CB} \tag{4}$$

To shed light on how Co doping boosts the tribocatalytic performance of NiO, EIS is employed to evaluate charge-transfer behavior [46]. As shown in Fig. 10(d), the capacitive arc radius of *x* wt% Co–NiO is reduced compared with that of NiO, indicating decreases in both the solid-state interfacial layer resistance and surface charge resistance. This reduction also lowers the electron transfer energy barrier, which enhances the charge transfer efficiency. Among the catalysts, 7 wt% Co–NiO exhibits a significantly smaller radius of the capacitive resistance arc than any other. This indicates that it possesses lower charge transfer resistance and superior charge carrier transfer efficiency, which is beneficial for catalytic performance [47].

The capacity of a material to accept or donate electrons can be assessed using the work function. In semiconductors, the work function is derived from the material's electron affinity energy, Fermi energy level, and the positioning of the valence and conduction bands. For p-type semiconductors, the figure of merit is computed as specified in Eq. (5) [48].

$$W_s = X + E_g - (E_{fs} - E_v) \tag{5}$$

where E_g is the band gap value; E_{fs} is the Fermi energy level; E_v is the valence band value; W_s is the work function; X is the electron affinity energy. As NiO is a p-type semiconductor, the Fermi energy level E_{fs} is situated near the valence band, resulting in $E_{fs} - E_v \approx 0$ [49]. The ionic radius of Co^{2+} (0.621 Å) exceeds that of Ni^{2+} (0.605 Å), and the incorporation of Co into NiO results in a marginal expansion of the crystal lattice, in accordance with the principle that an increase in atomic radius correlates with a decrease in electron affinity energy [50]. Thus, Co doping reduces the electron affinity, which is consistent with the experimental observation that Co–NiO has a narrower band gap than pure NiO. Consequently, Co doping reduces the work function of NiO, enhancing its electron donation capability and increasing the friction charge generated per unit area.

The photoluminescence (PL) spectra of NiO and 7 wt% Co–NiO are analyzed in the 300–700 nm region to further assess the impact of Co doping on carrier transport. Figure 11(a) illustrates that Co doping results in a substantial reduction in the photoluminescence intensity of NiO, suggesting that Co doping improves the separation efficiency of electron–hole pairs. The fluorescence lifetime of the sample is further calculated to compare the migration and separation of internal charges before and after doping by using Eq. (6) [51]:

$$\tau = (A_1\tau_1^2 + A_2\tau_2^2)/(A_1\tau_1 + A_2\tau_2) \tag{6}$$

where A_1 and A_2 are the pre-exponential factors, and τ_1 and τ_2 are the corresponding radiative lifetimes.

As shown in Fig. 11(b), the average fluorescence lifetimes of 7 wt% Co–NiO and NiO are 37.4913 and 4.5984 ns, respectively. This suggests that Co doping improves the separation efficiency of

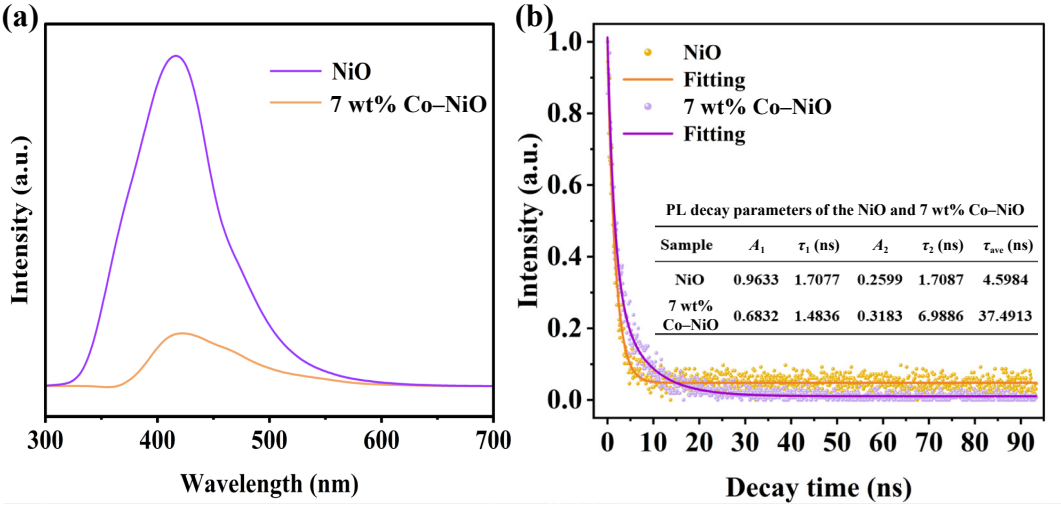

Fig. 11 (a) PL spectra and (b) time-resolved PL spectra of NiO and 7 wt% Co–NiO.

electron–hole pairs in NiO under mechanical excitation, leading to a carrier lifetime that is approximately 8 times longer.

5 Tribocatalytic mechanism

The function of active species in dye decomposition is evaluated by conducting scavenger tests using TBA, EDTA-2Na, and BQ for trapping OH, h^+, and $\cdot O_2^-$, respectively. As shown in Fig. 12, the decomposition ratios of RhB are 63%, 48.7%, and 92.4% with EDTA-2Na, BQ, and TBA addition, respectively. The accession of BQ gives rise to a remarkable decrease in the decomposition ratios of RhB, indicating that $\cdot O_2^-$ plays a major role in the tribocatalytic decomposition of RhB. However, it slightly decreases with EDTA-2Na addition, which indicates that h^+ plays a minor role in RhB decomposition. After the addition of TBA, the RhB decomposition ratio is almost unchanged. The results verify that the principal active species for RhB decomposition are $\cdot O_2^-$ and h^+, and that ·OH has no role.

Building on the evidence from radical trapping experiments, ESR analysis was performed to confirm the generation of active radicals in the tribocatalytic system [52]. As shown in Figs. 13(a)–13(c), no active species are observed without mechanical stirring. However, signals of $\cdot O_2^-$ and h^+ are detected after 30 min of stirring, while no ·OH signal appears, in agreement with prior trapping experiments that confirm that $\cdot O^{2-}$ and h^+ are formed instead of ·OH. This is because ·OH is generated by the direct oxidation of water molecules by h^+, which may react directly with dye molecules and participate in dye decomposition [53]. The absence of the ·OH signal is attributed to the Co–NiO VB potential (+0.57 V) being incapable of oxidizing OH^- or H_2O, which require redox potentials of +1.99 and +2.27 V, respectively [54]. In contrast, the CB potential of 7 wt% Co–NiO is −2.24 V, which exceeds the radical generation potential of $O_2/\cdot O_2^-$ −0.28 V and allows the catalyst's e^- to bond with O_2 to generate $\cdot O_2^-$ [55]. The highly oxidizing h^+ and $\cdot O_2^-$ produced by the tribocatalytic process further decompose the pollutants.

Referencing prior experimental research, the proposed possible tribocatalytic mechanism of Co–NiO nanoparticles for dye decomposition is plotted in Fig. 14. Triboelectrification is recognized as a universal phenomenon inherent in natural physical processes. When two materials contact each other, the reduction in interatomic distance results in overlapping electron clouds. Electron transfer between atoms is enabled by the lowered energy barrier resulting from overlapping electron clouds [56]. In this process, the material losing e^- acquires a positive charge, while

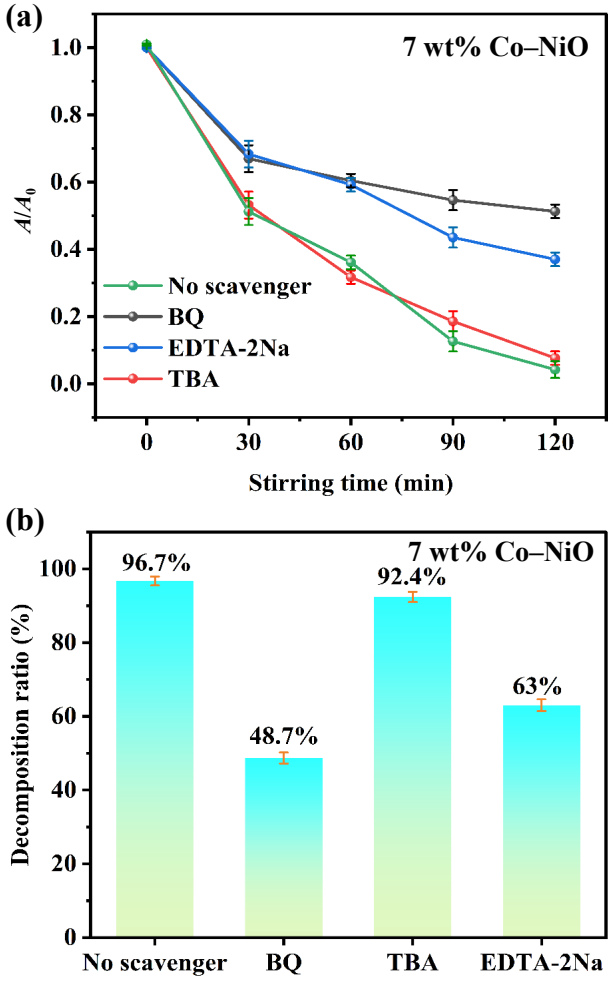

Fig. 12 (a) Kinetic study of RhB decomposition and (b) comparison of RhB decomposition ratios for 7 wt% Co–NiO with different radical scavengers.

the recipient gains a negative charge. Based on the triboelectric series and empirical law of triboelectricity, catalysts exhibit a higher electron affinity than PTFE, while PTFE tends to lose e^- more readily [57]. During mechanical stirring, the PTFE disk tightly contacts the beaker base under applied pressure. At the PTFE–beaker bottom interface, continuous friction occurs between the catalyst and PTFE, reducing their interatomic

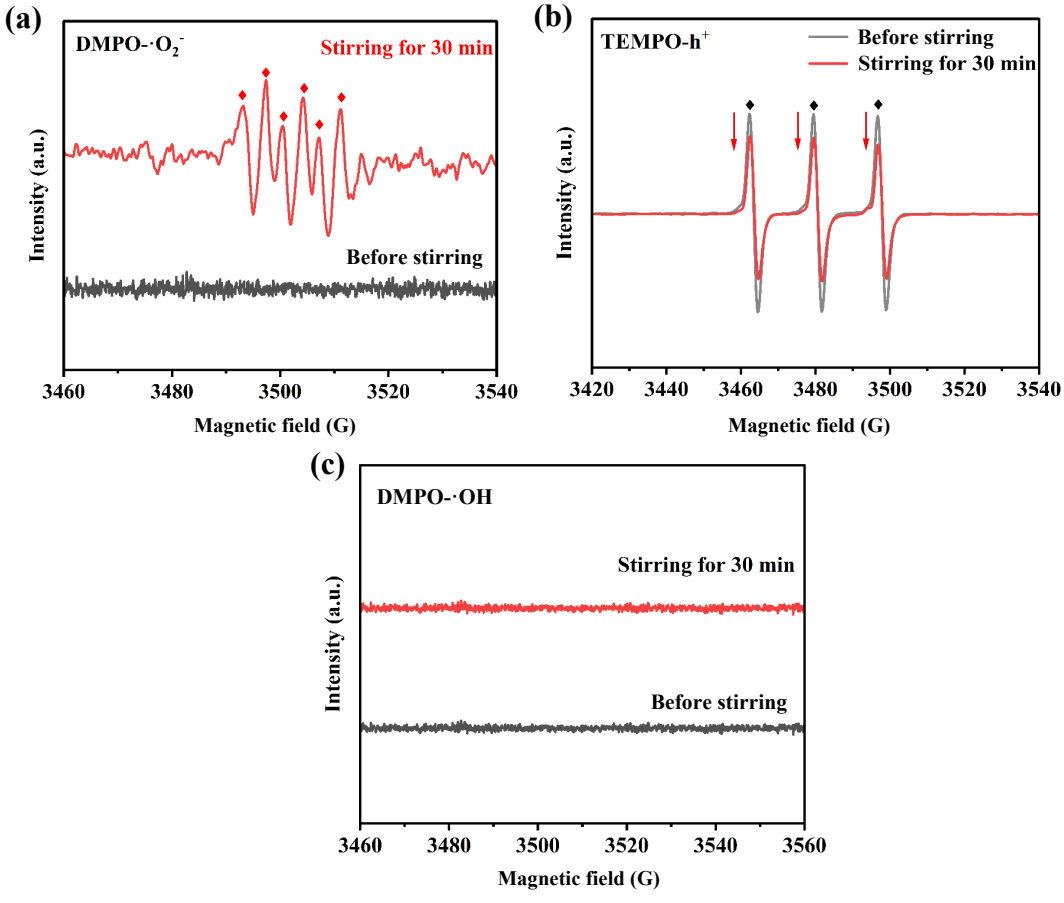

Fig. 13 ESR spectra of (a) $\cdot O_2^-$, (b) h^+, and (c) ·OH trapped by DMPO and TEMPO.

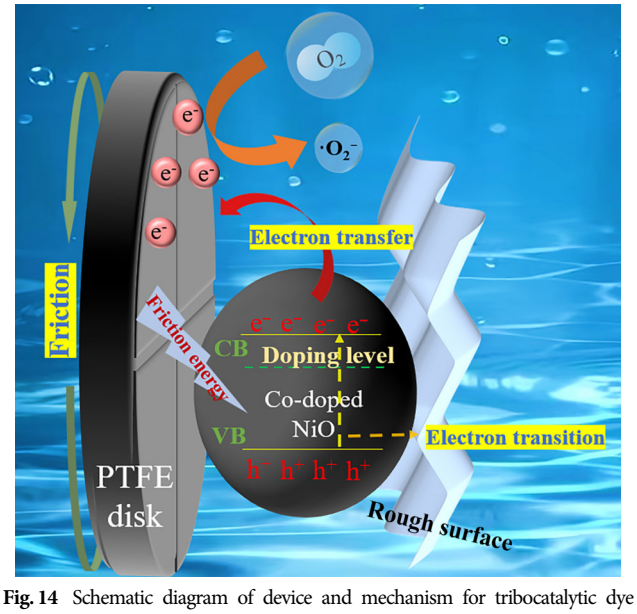

Fig. 14 Schematic diagram of device and mechanism for tribocatalytic dye decomposition using Co–NiO nanoparticles.

distance and causing electron cloud overlap. This diminished interatomic potential barrier facilitates electron transfer between the materials. Due to its higher electronegativity relative to the catalyst, PTFE preferentially attracts e^- during friction, resulting in electron migration from the catalyst surface to PTFE. Furthermore, the capacity to transport electrons during friction is influenced by the work function of the material. It is easier to donate electrons during frictional electricity when the work function is lower [58]. The impetus for electron transfer in triboelectricity arises from the disparity ($\Delta\Phi$) in work functions between the two materials, as expressed by Eq. (7) [59].

$$\Delta\Phi = \Phi_A - \Phi_B \tag{7}$$

where Φ_A and Φ_B denote the work functions of the respective materials. When $\Phi_A > \Phi_B$, electrons migrate from B to A, resulting in A being negatively charged and B being positively charged. When $\Phi_A < \Phi_B$, electrons migrate from A to B, resulting in A being positively charged and B being negatively charged. Due to the lower figure of merit of Co–NiO (4.54 eV) compared with that of PTFE (5.75 eV) [60], the binuclear electrons from Co–NiO are transferred to PTFE by friction, resulting in the Co–NiO and PTFE surfaces acquiring positive and negative charges, respectively.

The negative charges accumulated on the PTFE surface reduce dissolved O_2 to $\cdot O_2^-$ [61]. Furthermore, the Co–NiO nanoparticles absorb friction-derived mechanical energy, which excites electrons from the valence band to the conduction band. Although the holes left in the valence band by this process cannot oxidize OH^- to form ·OH, they directly participate in dye decomposition. In parallel, electrons in the conduction band react with dissolved O_2 to generate $\cdot O_2^-$, which subsequently contributes to dye decomposition.

The tribocatalytic dye decomposition process can be described by Reactions (8)–(11):

$$\text{Co}-\text{NiO nanoparticles} \xrightarrow{\text{Friction}} \text{Co}-\text{NiO nanoparticles} + h^+ + e^- \tag{8}$$

$$\mathrm{Co-NiO\ nanoparticles} + \mathrm{PTFE} \xrightarrow{\mathrm{Friction}} \mathrm{Co-NiO\ nanoparticles}(q^+) + \mathrm{PTFE}(q^-) \quad (9)$$

$$O_2 + e^- \rightarrow \cdot O_2^- \quad (10)$$

$$h^+ / \cdot O_2^- + \mathrm{Dyes} \rightarrow \mathrm{Decomposition} \quad (11)$$

6 Conclusions

In summary, NiO and x wt% Co–NiO nanoparticles were synthesized and utilized for the tribocatalytic decomposition of dyes. The findings show that the 7 wt% Co–NiO catalyst outperforms the others, decomposing 96.7 wt% of RhB within 120 min. This efficiency is 2.4 times higher than that of its undoped NiO. The incorporation of Co into NiO tailors its electronic band structure, sensitizing the material to external mechanical stimuli, thereby accelerating charge separation and interfacial electron transfer, and thereby collectively enhancing the tribocatalytic performance for dye decomposition. Additionally, after five cycles, the 7 wt% Co–NiO catalyst decomposes RhB up to 87.2%, indicating that the catalyst has good recovery stability. Mechanistic studies further showed that $\cdot O_2^-$ is the main active species responsible for decomposing RhB. This study's outcomes underscore the effective improvement of tribocatalyst performance through the incorporation of metal elements, and future work will continue to refine the design of more efficient tribocatalyst systems to broaden their applications.

Acknowledgements

This research was funded by the National Natural Science Foundation of China (Nos. 12474472 and 51902094), Shaanxi Province Natural Science Foundation (No. 2025JC-YBMS-158), Shaanxi Science and Technology Plan Projects of China (No. 2024NC-YBXM-169), Shaanxi Qinchuangyuan "Scientist + Engineer" Team Construction (No. 2025QCY-KXJ-018), Shaanxi Province High-level Talent Introduction Program (Youth Project), the Scientific Research Plan Projects of Shaanxi Education Department: Biological Resources Development and Textile Wastewater Treatment Innovation Team (No. 23JP055), Jiangxi Provincial Natural Science Foundation (No. 20252BAC240241), UKRI Postdoctoral Fellowship Guarantee (No. EP/Y017412/1), the Open Research Project of the Key Laboratory of Adsorption Treatment and Resource Utilization of Organic Wastewater in the National Petroleum and Chemical Industry (No. SDHY2301), and the Open Research Project of the Engineering Research Center for New Materials and Environmental Remediation in Chemical Adsorption and Separation (No. SDGC2305).

Availability of data and materials

The data that support the findings of this study are available from the corresponding author upon reasonable request.

Competing interests

The authors have no competing interests to declare that are relevant to the content of this article.

References

[1] Li YL, Yu XY, Zhou YJ, *et al.* Nanostructured ZnO/$BiVO_4$ I-scheme heterojunctions for piezocatalytic degradation of organic dyes via harvesting ultrasonic vibration energy. *Int J Min Met Mater* 2025, **32**: 488–497.

[2] Mohanty A, Parida S, Behera RK, *et al.* Vibration energy harvesting: A review. *J Adv Dielectr* 2019, **9**: 1930001.

[3] Ishwarya S, Nagaswarupa HP, Naik YV, *et al.* Multifunctional applications of barium zinc vanadate nanoparticles for photocatalytic dye degradation, energy storage and sensing applications. *Int J Min Met Mater* 2025, **32**: 3052–3071.

[4] Feng Y, Li JH, Yan H. Synthesis of $BiFeO_3$/ZnO heterojunction with enhanced piezocatalytic performance for highly-effective degradation of organic pollutant. *J Adv Dielectr* 2025, **15**: 2450023.

[5] Yuan JS, Zhang Y, Zhang XY, *et al.* Template-free synthesis of core–shell Fe_3O_4@MoS_2@mesoporous TiO_2 magnetic photocatalyst for wastewater treatment. *Int J Min Met Mater* 2023, **30**: 177–191.

[6] Ren QM, Chen P, Sun N, *et al.* Adjusting photocatalytic hydrogen production of TiO_2 hollow nanospheres through nitrogen-induced shallow trapping levels. *J Adv Dielectr* 2025, **15**: 2450005.

[7] Wu Z, Xu TS, Zhang LH, *et al.* Ferroelectric $BaTiO_3$/Pr_2O_3 heterojunction harvesting room-temperature cold–hot alternation energy for efficiently pyrocatalytic dye decomposition. *J Adv Ceram* 2024, **13**: 44–52.

[8] Wang Y, Xu XL, Xiao LB, *et al.* Balancing the piezoelectric coefficient and carrier concentration of Bi_2WO_{6-x} for ultrahigh piezocatalysis. *J Adv Ceram* 2024, **13**: 1737–1747.

[9] Ismail M, Wu Z, Zhang LH, *et al.* High-efficient synergy of piezocatalysis and photocatalysis in bismuth oxychloride nanomaterial for dye decomposition. *Chemosphere* 2019, **228**: 212–218.

[10] Guo D, Wu Z, Shu XX, *et al.* Strongly piezocatalytic dye decomposition of sol–gel synthesized PZT film. *Ceram Int* 2024, **50**: 2514–2520.

[11] Chen MZ, Jia YM, Li HM, *et al.* Enhanced pyrocatalysis of the pyroelectric $BiFeO_3$/g-C_3N_4 heterostructure for dye decomposition driven by cold-hot temperature alternation. *J Adv Ceram* 2021, **10**: 338–346.

[12] Li PC, Wu J, Wu Z, *et al.* Strong tribocatalytic dye decomposition through utilizing triboelectric energy of barium strontium titanate nanoparticles. *Nano Energy* 2019, **63**: 103832.

[13] Lei H, Cui XD, Jia XC, *et al.* Enhanced tribocatalytic degradation of organic pollutants by ZnO nanoparticles of high crystallinity. *Nanomaterials* 2023, **13**: 46.

[14] Mao CY, Zhang YC, Lei H, *et al.* Boosting tribo-catalytic degradation of organic pollutants by $BaTiO_3$ nanoparticles through metallic coatings. *Appl Surf Sci* 2024, **663**: 160172.

[15] Cui XD, Li PC, Lei H, *et al.* Greatly enhanced tribocatalytic degradation of organic pollutants by TiO_2 nanoparticles through efficiently harvesting mechanical energy. *Sep Purif Technol* 2022, **289**: 120814.

[16] Kumar M, Gaur A, Chauhan VS, *et al.* Tribocatalytic dye degradation using $BiVO_4$. *Ceram Int* 2024, **50**: 8360–8369.

[17] Gaur A, Kumar Moharana A, Porwal C, *et al.* Degradation of organic dyes by utilizing $CaCu_3Ti_4O_{12}$ (CCTO) nanoparticles via tribocatalysis process. *J Ind Eng Chem* 2024, **129**: 341–351.

[18] Ruan LJ, Jia YM, Guan JF, *et al.* Tribo-electro-catalytic dye degradation driven by mechanical friction using MOF-derived $NiCo_2O_4$ double-shelled nanocages. *J Clean Prod* 2022, **345**: 131060.

[19] Li YY, Yin YC, Bai Y, *et al.* Engineering the optical properties of $SrZrO_3$ crystals via Zn doping for superior passive daytime radiative cooling. *J Adv Ceram* 2025, **14**: 9221107.

[20] Mojallal S, Mohammadzadeh H, Aghaeinejad-Meybodi A, *et al.* Effect of NiO–$NiCr_2O_4$ nano-oxides on the microstructural, mechanical and corrosion properties of Ni-coated carbon steel. *Int J Min Met Mater* 2023, **30**: 1078–1092.

[21] Liu SY, Yang YD, Hu YM, *et al.* Effect of strontium substitution on the tribocatalytic performance of barium titanate. *Materials* 2023, **16**: 3160.

[22] Hu JL, Ma W, Pan YZ, *et al.* Insights on the mechanism of Fe doped

ZnO for tightly-bound extracellular polymeric substances tribo-catalytic degradation: The role of hydration layers at the interface. *Chemosphere* 2021, **276**: 130170.
[23] Yan MG, Liu TT, Hu YS, *et al.* Construction of $WO_3/ZnIn_2S_4$ Z-scheme heterojunction by electrostatic self-assembly to enhance charge separation and reactive oxygen species generation. *J Water Process Eng* 2026, **82**: 109445.
[24] Lei H, Jia XC, Wang HB, *et al.* Tribo-catalytic conversions of H_2O and CO_2 by NiO particles in reactors with plastic and metallic coatings. *Coatings* 2023, **13**: 396.
[25] Wang KQ, Li BX, Zhao CR, *et al.* A novel $NiO/BaTiO_3$ heterojunction for piezocatalytic water purification under ultrasonic vibration. *Ultrason Sonochem* 2023, **92**: 106285.
[26] Yu HJ, Wei XD, Wang M, *et al.* Macroscopic polarization enhancement boosting piezo-photocatalytic performance via Nb-doping on B-site of $Bi_4Ti_3O_{12}$ nanosheets. *J Adv Ceram* 2024, **13**: 437–446.
[27] Asaldoust F, Mabhouti K, Jafari A, *et al.* Structural, magnetic, and optical characteristics of undoped and chromium, iron, cobalt, copper, and zinc doped nickel oxide nanopowders. *Sci Rep* 2025, **15**: 1088.
[28] Zhang GM, Ge T, Zhang YC, *et al.* Hydrothermal preparation of Nb^{5+}-doped α-Fe_2O_3 nanorods for efficient visible light-driven photocatalytic reduction of hexavalent chromium. *Powder Technol* 2024, **436**: 119480.
[29] Yang ZQ, Wang X, Wang FJ, *et al.* Tribocatalytic activity of poled $BaCu_xTi_{1-x}O_{3-x}$ nanofibers for degradation of organic dye. *Adv Powder Technol* 2024, **35**: 104612.
[30] Shkir M, Palanivel B, Khan A, *et al.* Tailoring the structural, optical and remarkably enhanced photocatalytic activities of nickel oxide nanostructures through cobalt doping. *Surf Interfaces* 2021, **27**: 101515.
[31] Hamidian K, Zarin A, Sarani M, *et al.* Study of cytotoxic performance of green-synthesized Co doped NiO nanoparticles over human breast cancer cells. *Inorg Chem Commun* 2024, **162**: 112234.
[32] Huang GP, Dong W, Fang L, *et al.* Effects of Eu-doping site on structural and photoluminescent properties of $CaTiO_3$ particles. *J Adv Dielectr* 2011, **1**: 215–221.
[33] Yang ZK, Mu JX, Wang ZT, *et al.* Research on the influence of the morphology and crystal structure of NiO and Cu–NiO nanofilms on nonlinear absorption properties in the visible light band. *J Alloy Compd* 2025, **1032**: 180878.
[34] Zhang X, Chen Y, Liu ZQ, *et al.* Small and low-crystallinity NiO nanoparticles embedded in hollow carbon materials for high performance asymmetric supercapacitors. *J Energy Storage* 2025, **113**: 115738.
[35] Wang Y, Shen SS, Liu MY, *et al.* Enhanced tribocatalytic degradation performance of organic pollutants by $Cu_{1.8}S/CuCo_2S_4$ p–n junction. *J Colloid Interf Sci* 2024, **655**: 187–198.
[36] Cai WM, Sun XY, Bao YJ, *et al.* Distinct morphology-dependent behaviors for Au/γ-Al_2O_3 catalysts: Enhanced thermal stabilization in CO oxidation reaction. *RSC Adv* 2023, **13**: 9010–9019.
[37] Xu YJ, Meng YZ, Xiang X, *et al.* Modulating low-frequency tribocatalytic performance through defects in uni-doped and bi-doped $SrTiO_3$. *J Adv Ceram* 2024, **13**: 1153–1163.
[38] Yang B, Chen HB, Guo XD, *et al.* Enhanced tribocatalytic degradation using piezoelectric CdS nanowires for efficient water remediation. *J Mater Chem C* 2020, **8**: 14845–14854.
[39] Rafiq A, Ikram M, Ali S, *et al.* Photocatalytic degradation of dyes using semiconductor photocatalysts to clean industrial water pollution. *J Ind Eng Chem* 2021, **97**: 111–128.
[40] Wu Z, Wu SQ, Zhang LH, *et al.* Low-frequency contact-electro-catalysis driven by friction between the PTFE-coated fabric and dye solution. *J Alloy Compd* 2025, **1010**: 177440.
[41] Fan FR, Xie SJ, Wang GW, *et al.* Tribocatalysis: Challenges and perspectives. *Sci China Chem* 2021, **64**: 1609–1613.
[42] Wang LX, Dong YL, Zhang JY, *et al.* Construction of NiO/g-C_3N_4 p–n heterojunctions for enhanced photocatalytic CO_2 reduction. *J Solid State Chem* 2022, **308**: 122878.
[43] Liu XY, Fan BY, Wang ZH, *et al.* Dynamic internal field engineering in $BaTiO_3$–TiO_2 nanostructures for photocatalytic dye degradation. *ACS Appl Nano Mater* 2021, **4**: 3742–3749.
[44] Su XH, Li WJ, Chen D, *et al.* Rapid fabrication of oxygen-deficient zirconia by flash sintering treatment. *J Adv Ceram* 2024, **13**: 1881–1890.
[45] He ZP, Wang YH, Shang TQ, *et al.* $MgFe_2O_4$–$LaFeO_3$ photocatalyst activating persulfate for the efficient degradation of methyl orange. *J Liaocheng Univ Nat Sci Ed* 2025, **38**: 747–755. (in Chinese)
[46] Ali T, Warsi MF, Zulfiqar S, *et al.* Green nickel/nickel oxide nanoparticles for prospective antibacterial and environmental remediation applications. *Ceram Int* 2022, **48**: 8331–8340.
[47] Gu J, Li SS, Cui TY, *et al.* Preparation of biomass charcoal doped BiOBr and its photocatalytic performance. *J Liaocheng Univ Nat Sci Ed* 2025, **38**: 68–75. (in Chinese)
[48] Shao GS. Work function and electron affinity of semiconductors: Doping effect and complication due to Fermi level pinning. *Energy Environ Mater* 2021, **4**: 273–276.
[49] Michaelson HB. The work function of the elements and its periodicity. *J Appl Phys* 1977, **48**: 4729–4733.
[50] Sheena P A, Hitha H, Sreedevi A, *et al.* Microstructural characterization and modified spectral response of cobalt doped NiO nanoparticles. *Mater Chem Phys* 2019, **229**: 412–420.
[51] Ong WJ, Putri LK, Tan YC, *et al.* Unravelling charge carrier dynamics in protonated g-C_3N_4 interfaced with carbon nanodots as co-catalysts toward enhanced photocatalytic CO_2 reduction: A combined experimental and first-principles DFT study. *Nano Res* 2017, **10**: 1673–1696.
[52] Cui ZX, Zhang L, Xue YQ, *et al.* Effects of shape and particle size on the photocatalytic kinetics and mechanism of nano-CeO_2. *Int J Min Met Mater* 2022, **29**: 2221–2231.
[53] Nosaka Y, Nosaka AY. Generation and detection of reactive oxygen species in photocatalysis. *Chem Rev* 2017, **117**: 11302–11336.
[54] LaVerne JA. OH radicals and oxidizing products in the gamma radiolysis of water. *Radiat Res* 2000, **153**: 196–200.
[55] Lin XT, Sun F, Sun Q, *et al.* O_2/O_2^- crossover- and dendrite-free hybrid solid-state Na–O_2 batteries. *Chem Mater* 2019, **31**: 9024–9031.
[56] Huang XF, Xu XY, Yang RY, *et al.* Synergetic adsorption and photocatalysis performance of g-C_3N_4/Ce-doped MgAl-LDH in degradation of organic dye under LED visible light. *Colloid Surface A* 2022, **643**: 128738.
[57] Lin SQ, Xu C, Xu L, *et al.* The overlapped electron-cloud model for electron transfer in contact electrification. *Adv Funct Mater* 2020, **30**: 1909724.
[58] Yang J, Shao CY, Li XA, *et al.* Electrospinning preparation and photocatalytic performance of ceramic fibers. *Adv Ceram* 2024, **45**: 59–73. (in Chinese)
[59] Liu XY, Zhu GJ, Yan QC, *et al.* Work-function-engineered TiN/N-doped carbon heterostructure for accelerating lithium-ion transport in micron-sized SiO anodes. *Nano Lett* 2025, **25**: 17220–17229.
[60] Trigwell S, Grable N, Yurteri CU, *et al.* Effects of surface properties on the tribocharging characteristics of polymer powder as applied to industrial processes. *IEEE T Ind Appl* 2003, **39**: 79–86.
[61] Teng JY, Li WL, Wei Z, *et al.* Coupling photocatalytic hydrogen production with key oxidation reactions. *Angew Chem Int Edit* 2024, **63**: 202416039.